Materials Letters 356 (2024) 135605

Contents lists available at ScienceDirect

Materials Letters

journal homepage: www.elsevier.com/locate/matlet

Bimetallic structure of TZM and NbZr1 fabricated by wire-based directed energy deposition

Sainand Jadhav [a], Md Abdul Karim [a], Duck Bong Kim [b,*]

[a] Department of Mechanical Engineering, Tennessee Technological University, Cookeville, TN, USA
[b] Department of Manufacturing and Technology, Tennessee Technological University, Cookeville, TN, USA

ARTICLE INFO

Keywords:
Bimetallic structures
Refractory alloys
TZM-NbZr1
Wire-arc additive manufacturing

ABSTRACT

The outcome of this study highlights the feasibility of additively manufactured bimetallic structures from refractory alloys for high-temperature applications. Using a wire-based directed energy deposition (DED) process, a bimetallic structure composed of molybdenum alloy (TZM) and niobium alloy (NbZr1) was successfully fabricated. The TZM-NbZr1 interface displayed no significant defects, such as cracks or delamination, and showed no presence of intermetallic compounds. A few pores were observed on the deposited NbZr1 side near the interface. During uniaxial tensile testing, the specimen's failure occurred on the NbZr1 side in close proximity to the interface, resulting in an ultimate tensile strength of 249 ± 126 MPa and an elongation of less than 6 %.

1. Introduction

In today's advanced engineering applications, there is a demand for components with improved, tailored, and location-specific properties, which a bimetallic structure (BS) often could satisfy. By combining different metallic elements into a single structure, it can be a multifunctional component [1]. A BS made of refractory alloys, for instance, molybdenum-based titanium-zirconium-molybdenum (TZM) alloy and niobium-based niobium-zirconium (NbZr1) alloy, can be used in nuclear and aerospace applications requiring high-temperature operations. One challenge associated with the fabrication of TZM and NbZr1 is their high reactivity with atmospheric gases. According to the Mo-Nb binary phase diagram, Mo and Nb can't be completely miscible until the temperature reaches 2400 °C [2], which can make their manufacture difficult. Lin et al. [3] and Yang et al. [4] individually joined TZM to NbZr1 utilizing diffusion bonding and liquid metallic film bonding, respectively, using Ni interlayer. Yang et al. [5] adopted contact-reactive brazing to join TZM and Nb-Zr alloys with Ni interlayer.

In recent years, additive manufacturing (AM) has revolutionized the manufacturing industry through its rapid and complexity-free fabrication capabilities [6]. Wire-arc additive manufacturing (WAAM), a DED-based AM process, uses an electric arc and a wire as a deposition material [7]. The key advantages of WAAM are its low setup cost and its capacity to fabricate large-scale components [8]. The fabrication of a TZM-NbZr1 BS using the WAAM technique could broaden the scope of high-temperature applications. However, the feasibility of the additive manufacturing of TZM-NbZr1 BS is yet to be revealed. In this study, a WAAM process has been adopted to fabricate TZM-NbZr1 BS. The interfacial microstructure and the bonding strength have been examined. The outcome of this research could serve as a reference for future work on the AM of TZM-NbZr1.

2. Materials and methods

The deposition process was carried out with a gas tungsten arc welding (GTAW)-based WAAM system composed of a six-axis Fanuc ArcMate 120iC robot with a Fanuc R-J3iB controller, a Miller Dynasty 400 GTA welding power source, and a generic wire feeder. The consumable wire of NbZr1 (ASTM-B392) with a diameter of 0.95 mm was deposited on the TZM substrate of size 100 mm × 20 mm × 5 mm. The process parameters used in this study are shown in Fig. 1(a). After the deposition of each layer, the top surface was allowed to cool down to 200 °C before depositing the next layer. Fig. 1(b) shows the deposited thin-wall structure of TZM-NbZr1.

Using wire electrical discharge machining, the specimens for microstructure and mechanical property characterization were extracted from the deposited thin-wall, as shown in Fig. 1(b). The metallographic specimens were prepared using standard metallographic procedures. The TZM side and NbZr1 side were individually etched using Murakami's reagent and specially prepared etchant (10 mL HF +

* Corresponding author.
E-mail address: dkim@tntech.edu (D. Bong Kim).

https://doi.org/10.1016/j.matlet.2023.135605
Received 22 September 2023; Received in revised form 9 November 2023; Accepted 17 November 2023
Available online 19 November 2023

10 mL HNO_3 + 30 mL lactic acid), respectively. The microstructures were analyzed using Nikon SMZ100 and Nikon MA100 optical microscopes (OM) and a Hitachi SU7000 scanning electron microscope (SEM) coupled with energy dispersive spectrometry (EDS). X-ray diffraction (XRD) analysis was carried out utilizing the Rigaku Ultima IV machine to determine the phases at the TZM-NbZr1 interface. Microhardness tests were performed using a Buehler-Wilson VH1202 microhardness tester with a 500 g applied load and a dwell time of 10 s. Uniaxial tensile tests were executed on specimens with dimensions shown in Fig. 1(c) as per the ASTM E8 standard using a micromechanical test machine from TestResources, Inc.

3. Results and discussion

3.1. Microstructure

Fig. 2 exhibits the interfacial microstructure of TZM-NbZr1. No considerable cracks or delamination were identified at the interface. Non-uniformly distributed pores of various sizes can be observed in the deposited NbZr1 close to the interface, as shown in Fig. 2(b) and (c). This could be due to the oxidation of diffused molybdenum (Mo) from the TZM substrate to NbZr1. Because of its strong chemical affinity for oxygen, Mo forms volatile Mo oxides at temperatures above 700 °C [9]. Kaserer et al. [10] and Islam et al. [11] reported pore formation in TZM alloy from MoO_3 generation during AM. In other studies, similar types of pores were also observed in electron-beam-welded TZM sheets [12,13]. However, the formation of pores in this current study tends to decrease along the build direction of NbZr1 because of the gradual reduction of Mo concentration. The microstructure on the NbZr1 side comprises large columnar grains along the build direction (Fig. 2(a)), because this is the grain growth direction that is normal to the solid/liquid interface. The formation of columnar grains is due to the epitaxial growth of dendrites from the partially melted grains of the previously deposited layer [14]. The TZM substrate contains fine equiaxed grains, as shown in Fig. 2(b) and (c), which are typical microstructures of powder-metallurgy-based TZM components. The EDS line and point scan results at the interface are presented in Fig. 2(d)–(f). The composition of Mo and Nb varies significantly over the interface. It does not, however, demonstrate any appreciable fluctuation in the concentrations of Zr and Ti.

While a considerable quantity of Mo diffusion was observed into NbZr1, the Nb diffusion into the TZM side is insignificant. This is also evident in the EDS mapping shown in Fig. 3(a). This could be because the Mo diffusion coefficient in Nb is comparatively higher than the Nb diffusion coefficient in Mo [15]. XRD analysis at the interface of TZM-NbZr1 shown in Fig. 3(b). It shows the existence of pure Mo and Nb phases. However, no intermetallic compound (IMC) phases are evident. The formation of Mo-Nb IMCs is not energetically favorable, according to the binary phase diagram of the Mo-Nb system [2]. Major Nb peaks were found at 2-theta ~ 38.04°, 55.22°, 68.96°, and 81.86°, corresponding to the BCC crystal planes of (110), (200), (211), and (220), respectively, whereas major Mo peaks were observed at 2-theta ~ 40.14°, 58.25°, 73.28°, and 87.25°, corresponding to the BCC crystal planes of (110), (200), (211), and (220), respectively.

3.2. Mechanical property

The microhardness profile obtained from the substrate to the top of the deposit is presented in Fig. 4(a). The entire microhardness profile can be divided into 3 regions: the TZM side, the heat-affected zone (HAZ) in the TZM, and the NbZr1 side. On the TZM side, hardness was measured in the range of 226–253 HV, with an average hardness of 239 HV, which is consistent with the typical hardness value of TZM alloy processed by powder metallurgy [16]. In the HAZ of TZM, an average hardness of 197 HV was observed. According to Zhang et al. [12], owing to the recrystallization produced in HAZ of TZM alloy, the mechanical hardening would disappear in HAZ, which may result in lower hardness. The hardness value adjacent to the interface on the NbZr1 side increased to 231 HV, which could be attributed to the migration of Mo from TZM to the NbZr1 side. In general, the Mo element is harder than the Nb element. The hardness value gradually decreased to an average of 160 HV on the NbZr1 side due to the progressive reduction of Mo content. However, the hardness further increased to about 210 HV in the top layers of deposited NbZr1. A prior study observed a similar trend in hardness distribution for NbZr1 fabricated through WAAM. The authors noted increased hardness in the top layers, attributing it to the reduction in secondary dendritic arm spacing (SDAS). This decrease in SDAS, caused by faster cooling at the top layers, correlates with increased hardness [17].

Fig. 4(b) presents the stress–strain curves for TZM-NbZr1 BS. The tensile strengths of 195 MPa, 393 MPa, and 158 MPa were measured for specimens S1, S2, and S3, respectively. The specimens experienced a low elongation of less than 6 %. Fig. 4(c)–(h) illustrates the SEM images and EDS point analysis of fracture surfaces. The specimens were fractured on the NbZr1 side, slightly above the TZM-NbZr1 interface. The EDS point analysis showed the presence of both Mo and Nb, with a higher percentage of Nb. All the specimens failed in a brittle manner. Specimens S1 and S3 experienced mixed *trans*-granular and intergranular fractures with river-like and rock candy morphologies. However, specimen S2 presented only a *trans*-granular fracture with a river-like pattern. No significant pores were identified in the fracture surface of specimen S2 that contributed to its comparatively higher strength. The non-uniformly distributed pores can be observed on the fracture surfaces

(a) Process parameter	Value
Electrode-to-workpiece distance	5mm
Tungsten electrode tip angle	45°
Torch angle	90°
Diameter of the electrode	4mm
Torch shielding gas	99.999% Ar
Shielding gas flow rate	15L/min
Wire feed rate	150cm/min
Torch speed	20cm/min
Current	200A

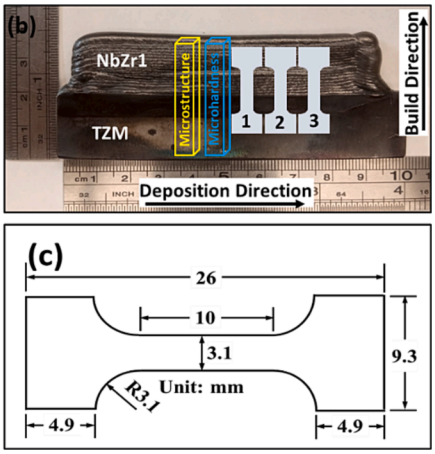

Fig. 1. (a) Process parameters, (b) thin-wall structure of TZM-NbZr1, and (c) geometry and dimensions of tensile specimen.

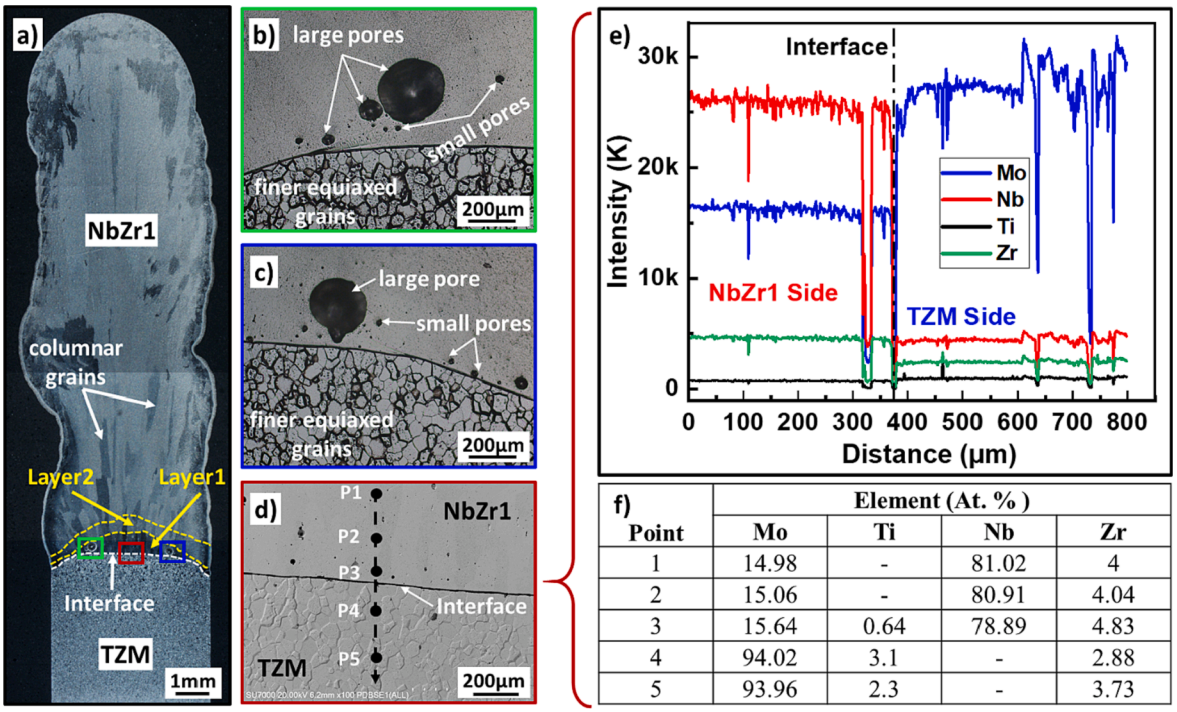

f)

Point	Element (At. %)			
	Mo	Ti	Nb	Zr
1	14.98	-	81.02	4
2	15.06	-	80.91	4.04
3	15.64	0.64	78.89	4.83
4	94.02	3.1	-	2.88
5	93.96	2.3	-	3.73

Fig. 2. (a)–(d) Microstructure; (e) EDS line scan; and (f) EDS point scan results of TZM-NbZr1 BS.

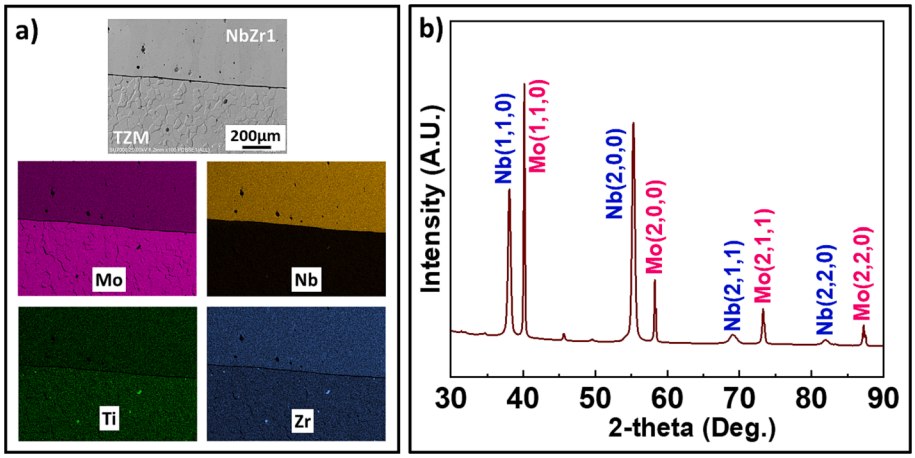

Fig. 3. (a) SEM micrograph of the interface with elemental area mapping; (b) XRD analysis results across the interface.

of specimens S1 and S3. A large variation in tensile strength was observed among the three specimens because of the non-uniformly distributed pores. The pores can act as a site of crack initiation under loading conditions. Cracks generated by the pores can expand and subsequently lead to the final fracture of the structure. However, further investigations into the pore formation mechanism and its elimination are required to enhance the mechanical properties.

4. Conclusions

A TZM-NbZr1 bimetallic structure was successfully fabricated using a GTAW-based WAAM process. Few non-uniformly distributed pores were observed in the deposited NbZr1 adjacent to the TZM-NbZr1 interface due to the oxidation of diffused Mo content from the TZM alloy. No intermetallic phases were formed at the interface. The ultimate tensile strength of 249 ± 126 MPa was achieved with an elongation of less than 6 %. A large standard deviation in strengths was observed due to the presence of non-uniformly distributed pores at the fracture locations. All specimens fractured in the deposited NbZr1 near the TZM-NbZr1 interface. Both *trans*-granular and intergranular brittle fractures were observed.

CRediT authorship contribution statement

Sainand Jadhav: Methodology, Data curation, Investigation, Visualization, Writing – original draft. **Md Abdul Karim:** Validation, Writing – review & editing. **Duck Bong Kim:** Conceptualization, Writing – review & editing, Resources, Supervision, Project administration, Funding acquisition.

Declaration of Competing Interest

The authors declare that they have no known competing financial interests or personal relationships that could have appeared to influence

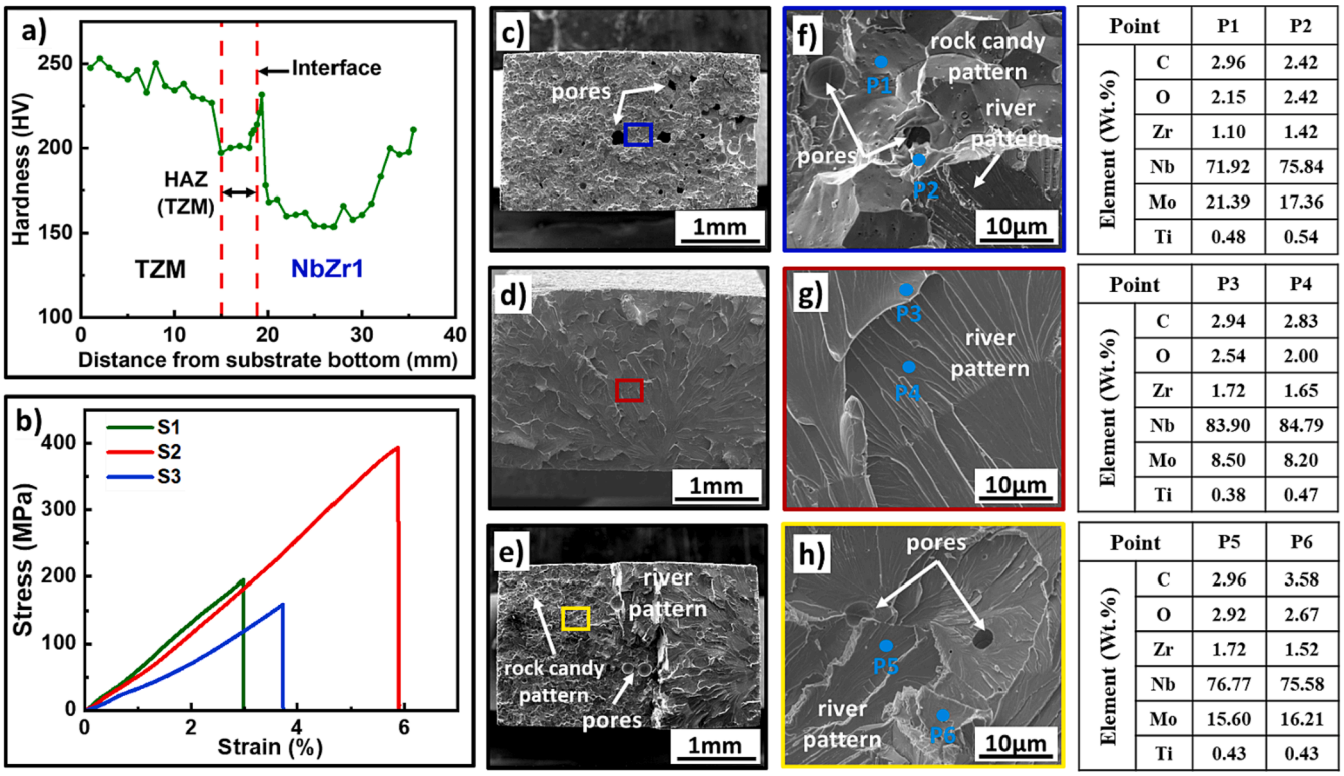

Point		P1	P2
Element (Wt.%)	C	2.96	2.42
	O	2.15	2.42
	Zr	1.10	1.42
	Nb	71.92	75.84
	Mo	21.39	17.36
	Ti	0.48	0.54

Point		P3	P4
Element (Wt.%)	C	2.94	2.83
	O	2.54	2.00
	Zr	1.72	1.65
	Nb	83.90	84.79
	Mo	8.50	8.20
	Ti	0.38	0.47

Point		P5	P6
Element (Wt.%)	C	2.96	3.58
	O	2.92	2.67
	Zr	1.72	1.52
	Nb	76.77	75.58
	Mo	15.60	16.21
	Ti	0.43	0.43

Fig. 4. (a) Hardness profile of BS; (b) stress–strain curve; (c)–(h) fracture surface morphologies and point scan results.

the work reported in this paper.

Data availability

Data will be made available on request.

Acknowledgements

The authors of this paper acknowledge the Center for Manufacturing Research (CMR) and Tennessee Technological University's Department of Manufacturing and Engineering Technology for their support. This material is based upon work supported by the National Science Foundation under Grant No. 2141905.

References

[1] A. Bandyopadhyay, et al., Virtual Phys. Prototyp. 17 (2022) 256–294, https://doi.org/10.1080/17452759.2022.2040738.
[2] C. Zhang, et al., Calphad. 51 (2015) 104–110, https://doi.org/10.1016/j.calphad.2015.09.001.
[3] J. Lin, et al., J. Alloys Compd. 743 (2018) 780–788, https://doi.org/10.1016/j.jallcom.2018.01.162.
[4] Z. Yang, et al., J. Song, J. Mater. Sci. Technol. 84 (2021) 16–26. https://doi.org/10.1016/j.jmst.2020.09.054.
[5] Z. Yang, et al., J. Manuf. Process. 57 (2020) 817–827, https://doi.org/10.1016/j.jmapro.2020.07.042.
[6] A. Beltagui, et al., Int. J. Prod. Econ. 255 (2023), 108677, https://doi.org/10.1016/j.ijpe.2022.108677.
[7] K. Treutler, et al., Appl. Sci. 11 (2021) 8619, https://doi.org/10.3390/app11188619.
[8] I. Ferreira, et al., J. Manuf. Technol. Manag. 34 (2023) 187–211, https://doi.org/10.1108/JMTM-06-2022-0235.
[9] Smolik, et al., J. Nucl. Mater. 283 (2000) 1458–1462. https://doi.org/10.1016/S0022-3115(00)00303-2.
[10] L. Kaserer, et al., Int. J. Refract. Metals Hard Mater. 93 (2020), 105369, https://doi.org/10.1016/J.IJRMHM.2020.105369.
[11] S. Islam, et al., Int. J. Refract. Metals Hard Mater. 110 (2023), 106042, https://doi.org/10.1016/J.IJRMHM.2022.106042.
[12] Y. Zhang, et al., Mater. Sci. Eng. A 700 (2017) 512–518, https://doi.org/10.1016/J.MSEA.2017.05.076.
[13] M. Stutz, et al., Mater. Sci. For. 879 (2017) 1865–1869, https://doi.org/10.4028/WWW.SCIENTIFIC.NET/MSF.879.1865.
[14] Ahsan, et al., J. Mater. Sci. Technol. 74 (2021) 176–188, https://doi.org/10.1016/J.JMST.2020.10.001.
[15] S. Prasad, et al., Metall. Mater. Trans. A Phys. Metall. Mater. Sci. 40 (2009) 1512–1514, https://doi.org/10.1007/s11661-009-9861-x.
[16] https://www.albmaterials.com/metals-and-alloys/783-tzm-molybdenum-alloy-sheets.html.
[17] S. Islam, et al., Adv. Eng. Mater. 25 (2023) 2201633, https://doi.org/10.1002/ADEM.202201633.